Locating boosted Kerr and Schwarzschild apparent horizons

Mijan F. Huq
J.P. Morgan-Chase, 270 Park Avenue, New York, New York 10017

Matthew W. Choptuik
CIAR Cosmology and Gravity Program, Department of Physics and Astronomy, University of British Columbia, Vancouver, British Columbia, Canada V6T 1Z1
and Center for Relativity, The University of Texas at Austin, Austin, Texas 78712-1081

Richard A. Matzner
Center for Relativity, The University of Texas at Austin, Austin, Texas 78712-1081
(Received 26 January 2000; published 30 October 2002)

We describe a finite-difference method for locating apparent horizons in generic spacetimes and illustrate its capabilities on boosted Kerr and Schwarzschild black holes. Our model spacetime is given by the Kerr-Schild metric. We apply a Lorentz boost to this spacetime metric and then carry out a $3+1$ decomposition. The result is a slicing of Kerr-Schwarzschild spacetime in which the black hole is propagated and Lorentz contracted. We show that our method can locate distorted apparent horizons efficiently and accurately.

DOI: 10.1103/PhysRevD.66.084024 PACS number(s): 04.70.Bw, 04.25.Dm

I. INTRODUCTION

Apparent horizon locators play an integral role in the application of black hole excision techniques to computational evolutions of black hole spacetimes. The idea behind excision techniques is to delete those regions of spacetime containing curvature singularities from the computational domain. This approach is viable since, assuming cosmic censorship, such curvature singularities are expected to be located within event horizons. By definition, an event horizon is a causal boundary whose interior does not causally affect the exterior spacetime; as a result it is possible to excise a region within the event horizon—including the black hole singularity—yet still be able to faithfully compute the geometry of the spacetime outside the black hole.

In our approach to computationally solving the Einstein field equations we focus on the use of Cauchy techniques, in which a $3+1$ splitting of spacetime into a foliation of spacelike hypersurfaces Σ, parametrized in time, is the basis for an evolution in time. The result of this splitting is a system of elliptic and hyperbolic partial differential equations in the 3-metric γ_{ij} and extrinsic curvature K_{ij}. These are the four constraint equations and 12 first-order-in-time evolution equations. The Cauchy approach starts with an initial spacelike slice with γ_{ij} and K_{ij} set by solving an initial value problem (the elliptic constraint equations). One then uses the evolution equations to evolve to the next spacelike slice obtaining γ_{ij} and K_{ij} at the next time (see York [1] for a detailed discussion).

In the evolution of black hole spacetimes in this manner we do not have a complete history of the entire spacetime and hence do not have knowledge of the location of the event horizon. Since the event horizon is a global object that depends on geometric information for all time (or at least until the black hole becomes quiescent) we cannot use it to determine an inner excision boundary in our Cauchy evolution. However, there is an alternative, and that is to use the apparent horizon surface which is a local object, locatable (if it exists) with γ_{ij} and K_{ij} on one time slice. The apparent horizon is the outermost marginally trapped surface. It is a closed spacelike 2-surface whose future-directed outgoing null normals have zero divergence [2]. The apparent horizon is slicing dependent and may not necessarily exist even though an event horizon does. An example of this is given by Wald and Iyer [3] through nonspherically symmetric slicings of the Schwarzschild spacetime. Provided a *non-pathological* slicing is chosen the apparent horizon or any trapped surface within it may be used for excising the black hole singularity. These surfaces define a local causal structure that distinguishes instantaneously escaping null rays from those that are certain to collapse. This distinction makes their treatment very amenable to computational black hole excision techniques. Since these surfaces can be determined with geometric information at one instant of time, they are used in practice as an inner boundary in Cauchy evolutions. With this purpose in mind, we developed a 3D apparent horizon locator that utilizes γ_{ij} and K_{ij} on a given spacelike slice of spacetime and locates an apparent horizon. Once it is located a region contained within it is excised. Thus the method is really a trapped-surface excision.

There has been a variety of work done on apparent horizon location in spherical symmetry, axisymmetry and 3D. We focus solely on the 3D locators. These can be classified into those that use finite difference methods, and those that utilize pseudo-spectral schemes. Further, one can classify each of these finders in terms of those that use flow methods versus those that directly solve the apparent horizon equation either via a minimization scheme or Newton's method for root finding.

One of the first published 3D apparent horizon locators was developed by Nakamura *et al.* [4]. Their method expands the *apparent horizon shape function*, $r=\rho(\theta,\phi)$, in spherical harmonics to some maximum $l=l_{\max}$:

$$\rho(\theta,\phi)=\sum_{l=0}^{l_{\max}}\sum_{m=-l}^{l} a_{lm}Y_{lm}(\theta,\phi). \tag{1}$$

With this expansion Nakamura *et al.* evaluate the apparent horizon equation and solve for the coefficients a_{lm} via a ''direct'' functional iteration scheme. Bishop [5] reimplemented this approach and made modifications that led to improved convergence and stability behavior. Anninos *et al.* [6] and Baumgarte *et al.* [7] implement similar methods that involve an expansion of $\rho(\theta,\phi)$; the primary differences in these later works is that they expand in terms of symmetric trace-free tensors and use Powell's method for minimization of the square of the apparent horizon equation [Eq. (2)], which is related to the expansion of the outgoing null normals.

Thornburg [8] gives a very good treatise on the use of finite differencing to solve the apparent horizon equation using spherical coordinates (r,θ,ϕ) via Newton's method. He discusses in general how algebraic Jacobians may be applied in a full 3D context. His implementation for horizon finding is, however, axisymmetric; his full 3D finder suffers from problems with the z axis ($\theta=0,\pi$). Our method for finding horizons uses closely related concepts except that we use finite differences in Cartesian coordinates, eliminating any potential z-axis problems.

Another class of apparent horizon locators casts the elliptic apparent horizon equation into a parabolic one as suggested by Tod [9], via the use of flow methods in locating apparent horizons. Bernstein [10] implemented Tod's algorithm in axisymmetry using finite differences, but encountered problems with differencing on a sphere in spherical coordinates in the general case.

The advantage of flow methods is that one can start with an arbitrary initial guess and flow towards the apparent horizon(s). In some implementations it is possible to find multiple apparent horizon surfaces starting from a single initial guess surface (i.e., there is a topology change in the course of location of the apparent horizon). Pasch [11] uses a level-set method to locate multiple apparent horizons in 3D. He demonstrates his method utilizing time-symmetric conformally flat initial data for multiple black holes. A hybrid flow or level-set-like method utilizing our approach of evaluating the outgoing null expansions via Cartesian finite differences has been implemented by Shoemaker *et al.* [12]. That method flows towards the apparent horizon(s) from an arbitrary initial guess allowing for topology changes. Gundlach [13] has implemented a ''fast flow'' method for finding apparent horizons. Alcubierre *et al.* [14] present a series of results for the pseudo-spectral method and the fast flow method for a series of ''testbed'' data sets.

In the sections that follow we give a brief discussion of the algorithm used and relegate the details to the Appendix. The model spacetime in which all of the results are presented is discussed in Sec. III. In Sec. IV we discuss tests of the algorithm and demonstrate that the algorithm fares well for distorted apparent horizons in boosted Kerr spacetimes.

II. FORMULATION AND SOLUTION OF THE ELLIPTIC PDE

On a particular 3D spacelike hypersurface, Σ, from our foliation of spacetime, we are given the 3-metric, γ_{ij} and the extrinsic curvature, K_{ij}. Let $\mathcal{S}$ be a closed 2-surface in Σ. At any point p on $\mathcal{S}$ we can define an outward-pointing spacelike normal, s^a, to $\mathcal{S}$, and a future-directed timelike normal, n^a, to Σ. From these we can construct the outgoing null normal, $k^a \equiv t^a + s^a$, at p. If the divergence $\nabla_a k^a$ (∇_a is the covariant derivative compatible with the spacetime metric, g_{ab}) is zero *everywhere* on $\mathcal{S}$, then $\mathcal{S}$ is a *marginally trapped surface* (MTS). The apparent horizon is the outermost such MTS. The equation for the vanishing of the divergence (expansion) of the outgoing null normals, $\nabla_a k^a = 0$, can be rewritten entirely in terms of quantities defined on Σ [1]:

$$D_i s^i + K_{ij} s^i s^j - K = 0. \tag{2}$$

Here D_i is the covariant derivative compatible with the 3-metric γ_{ij} and K is the trace of the extrinsic curvature.

Given a specific coordinatization of the 2-surface $\mathcal{S}$, the apparent horizon equation becomes an elliptic partial differential equation. This can be made manifest by noting that a MTS is a closed 2-surface; spherical coordinates thus provide a natural labelling of points on $\mathcal{S}$. The embedding of $\mathcal{S}$ in Σ can then be expressed in terms of the radial displacement, $\rho(\theta,\phi)$, measured from some origin in the interior of $\mathcal{S}$. In general one can generate a foliation of such closed spacelike 2-surfaces parametrized by their distance, φ, from the MTS:

$$\varphi(r,\theta,\phi) \equiv r - \rho(\theta,\phi). \tag{3}$$

Clearly, the $\varphi = 0$ level surface is the MTS. From this scalar function φ we can construct the outward-pointing spacelike vector field, s^i, which is normal to the constant-φ surfaces:

$$s^i = \gamma^{ij}\partial_j\varphi / \sqrt{\gamma^{kl}\partial_k\varphi\partial_l\varphi}. \tag{4}$$

Substitution of the above expression into Eq. (2) results in a second order elliptic partial differential equation on $\mathcal{S}$,

$$\begin{aligned} F[\rho] = {} & \gamma^{ab}\partial_a\partial_b\varphi + \gamma^{ab}_{\ ,a}\partial_b\varphi - \frac{1}{2}\omega^{-1}\gamma^{ab}\gamma^{cd}_a\partial_b\varphi\partial_c\varphi\partial_d\varphi \\ & - \omega^{-1}\gamma^{ab}\gamma^{cd}\partial_b\varphi\partial_a\partial_c\varphi\partial_d\varphi + \Gamma^a_{ab}\gamma^{bc}\partial_c\varphi \\ & + \omega^{-1/2}K_{ab}\gamma^{ac}\gamma^{bd}\partial_c\varphi\partial_d\varphi - \omega^{1/2}K = 0, \end{aligned} \tag{5}$$

which, as we have indicated, is to be interpreted as an equation for $\rho(\theta,\phi)$ and where $\omega = \gamma^{cd}\partial_c\varphi\partial_d\varphi$, and $\Gamma^a_{\ bc}$ are the connection coefficients associated with the 3-metric γ_{ab}.

Our approach involves the direct solution of Eq. (5) using finite-difference techniques and a global Newton iteration. To that end, $\mathcal{S}$ is replaced with a uniform finite-difference mesh, $\hat{\mathcal{S}}$, containing $N_\theta \times N_\phi$ points where $N_\theta = N_\phi = N_s$. (Note that here and below we adopt the notation whereby a discrete version of a continuum quantity, T, is denoted by $\hat{T}$.) The range of coordinates on $\hat{\mathcal{S}}$ is $0 \leqslant \theta \leqslant \pi$ and $0 \leqslant \phi < 2\pi$.

At the poles, $\theta=0$ and $\theta=\pi$, all N_ϕ points are identified. The $\phi=2\pi$ branch cut is identified with the $\phi=0$ line. The ''boundary conditions'' are periodicity at $\phi=2\pi$ and ϕ identification at $\theta=0,\pi$. These conditions are key to dealing with the coordinate singularities at the poles in combination with the use of *Cartesian* coordinates to discretize partial derivatives on $\hat{\mathcal{S}}$. We treat φ as a function of Cartesian coordinates x,y,z and center on each mesh point of $\hat{\mathcal{S}}$ a 3D Cartesian difference stencil of 27 points. Using the form Eq. (3) we interpolate values of $\varphi(x,y,z)$ onto each of the 26 stencil points surrounding each $\hat{\mathcal{S}}$ stencil point. (See the Appendix for more details.) Using this difference stencil we can evaluate first, second and mixed derivatives of $\varphi(x,y,z)$ as required by the discretized version of Eq. (5). At every point on $\hat{\mathcal{S}}$ we can then construct the residual $\hat{F}[\hat{\rho}]$ on $\hat{\mathcal{S}}$.

The problem at hand is to solve for $\rho(\theta,\phi)$ that yields $F[\rho]=0$. Since $F[\rho]$ is a nonlinear operator [as shown in Eq. (5)], we use a global Newton iteration, with an approximately computed Jacobian, to determine ρ. Given an initial guess surface, $\rho=\rho_0$, we wish to find a $\delta\rho$ (the change in the surface) that leads to $F[\rho_0+\delta\rho]=0$ or, to lowest order,

$$F[\rho_0+\delta\rho]=F[\rho_0]+\frac{\partial F[\rho]}{\partial\rho}\Big|_{\rho=\rho_0}\delta\rho+O(\delta\rho^2)=0. \quad (6)$$

Now, J defined by

$$J\equiv\frac{\partial F}{\partial\rho}. \quad (7)$$

is the Jacobian associated with F, and in the discrete case, $\hat{J}$ is an $N\times N$ matrix, where N is the total number of points used in the discretization. To obtain a $\delta\rho$ that gives $F[\rho+\delta\rho]=0$ to leading order, we must solve

$$J\cdot\delta\rho=-F[\rho] \quad (8)$$

for $\delta\rho$.

Computationally, each iteration of the Newton method involves (1) the evaluation of the discrete form of the Jacobian matrix, $\hat{J}$ and (2) the solution of the discrete form of Eq. (8). We numerically compute the Jacobian matrix by perturbing the surface pointwise and examining the effect of the perturbation on the residual, $\hat{F}$. Let $\overline{\mu}$ label ''independent'' points in the computational mesh, $\hat{\mathcal{S}}$. By independent we mean the unique points in the mesh, that is mesh-points modulo boundary identifications. In particular, given the identifications discussed above, there are $N\equiv N_s^2-2N_s+2$ independent points in $\hat{\mathcal{S}}$, since $N_s=N_\theta=N_\phi$ points at each of the poles are identified. Equation (8) then becomes a linear system of equations where $\hat{J}$ is an $N\times N$ matrix and $\hat{F}$ and $\delta\hat{\rho}$ are length-N vectors. The $\overline{\mu\nu}$ component of the Jacobian is then computed by perturbing $\hat{\rho}$ at the $\overline{\nu}$th point and computing the change in the residual, $\hat{F}$ at the $\overline{\mu}$th point. Specifically, using a first order forward difference approximation we calculate

$$\hat{J}_{\overline{\mu\nu}}\approx\frac{1}{\epsilon}\{\hat{F}_{\overline{\mu}}[\hat{\rho}_{\overline{\nu}}+\epsilon]-\hat{F}_{\overline{\mu}}[\hat{\rho}_{\overline{\nu}}]\}, \quad (9)$$

where ϵ, which we will call the *perturbation parameter*, is the amount by which we perturb the surface. We note that the process of generating the non-vanishing Jacobian elements involves an evaluation of $\hat{F}$ in only a small neighborhood of the νth point since $\hat{F}$ has a local domain of dependence (dependent on the discrete operators used, in our case these are finite differences convolved with interpolations). Notably, the computational cost for the Jacobian computation is $O(N)$, and the Jacobian has $O(N)$ non-zero elements.

Once we have solved the linear system for $\delta\hat{\rho}$, the estimate of $\hat{\rho}$ is updated via $\hat{\rho}=\hat{\rho}-\delta\hat{\rho}$, and the Newton iteration is repeated until the solution is deemed converged. In practice we demand that the L_2 norm of the change of the solution, $\|\delta\hat{\rho}\|_2$ [15], be driven below a chosen stopping criterion.

Further implementation details concerning our method are found in the Appendix. We now direct attention to the model spacetime which we use for our numerical experimentation with the technique.

III. 3+1 SPLITTING OF THE KERR-SCHILD METRIC

In the remainder of the paper we focus on tests of our algorithm which use Kerr black holes (including the limiting case of Schwarzschild black holes). The particular form of the Kerr solution that we use is the Kerr-Schild line element:

$$g_{\mu\nu}=\eta_{\mu\nu}+2Hl_\mu l_\nu, \quad (10)$$

where l_μ is an ingoing null vector (i.e. $g^{\mu\nu}l_\mu l_\nu=\eta^{\mu\nu}l_\mu l_\nu=0$), H is a scalar function of the spacetime coordinates and $\eta_{\mu\nu}$ is the Minkowski spacetime metric. We note that the above form of the Kerr metric is form invariant under a Lorentz transformation. By definition such a transformation takes $\eta_{\mu\nu}\rightarrow\eta_{\mu\nu}$ and l^μ and H are transformed to a new null vector and left unchanged (though evaluated at the new coordinate labels for the same event), respectively. This property makes our analysis easier since a $3+1$ decomposition of Eq. (10) has the same form as a $3+1$ decomposition of the boosted metric. As we shall see, we only need to specify H, l_μ and their spacetime derivatives in order to obtain the 3-metric and extrinsic curvature on Σ.

We also note that l^μ is the tangent field to a family of ingoing null geodesics, and thus Eq. (10) leads to a $3+1$ slicing of Kerr spacetimes that is well behaved at the horizon. That is, spacelike slices penetrate the horizon and hit the black hole singularity. This is a desirable property for black hole excision in computational applications and, indeed, this metric has proved to be a good choice for the study of single and multiple black hole evolutions with exicision.

Adopting ''Cartesian'' coordinates (t,x,y,z), H and l_μ are given by

$$H=\frac{Mr^3}{r^4+a^2z^2} \quad (11)$$

and

$$l_\mu = \left(1, \frac{rx+ay}{r^2+a^2}, \frac{ry-ax}{r^2+a^2}, \frac{z}{r}\right), \tag{12}$$

where r is given by

$$\frac{x^2+y^2}{r^2+a^2} + \frac{z^2}{r^2} = 1, \tag{13}$$

or

$$r^2 = \frac{1}{2}(\rho^2 - a^2) + \sqrt{\frac{1}{4}(\rho^2-a^2)^2 + a^2 z^2}. \tag{14}$$

In the above, M is the mass of the Kerr black hole, $a = J/M$ is the hole's angular momentum, and $\rho \equiv \sqrt{x^2+y^2+z^2}$.

In the $a \to 0$ limit we recover the Schwarzschild metric in ingoing Eddington-Finkelstein coordinates wherein

$$H = \frac{M}{r}, \tag{15}$$

$$l_\mu = \left(1, \frac{x}{r}, \frac{y}{r}, \frac{z}{r}\right) \tag{16}$$

and $r = \sqrt{x^2+y^2+z^2}$.

In a $t = \text{const}$ slice of a Kerr (or Schwarzschild) spacetime, the apparent horizon is known to coincide with the intersection of the event horizon with that slice. In the Kerr spacetime, then, the apparent horizon is a surface of radius $r = r_+$:

$$r_+ = M + \sqrt{M^2 - a^2} \tag{17}$$

and area

$$A = 4\pi(r_+^2 + a^2). \tag{18}$$

In the more general nonstationary case the apparent horizon and event horizon will not coincide. We thus emphasize that we use the special properties of the Kerr and Schwarzschild spacetimes described here solely to test and calibrate our scheme for locating apparent horizons.

To get the spacetime metric for a boosted Kerr hole, consider $\bar{\mathcal{O}}$ to be the rest frame of the black hole, with coordinates $(\bar{t}, \bar{x^i})$. Let $\mathcal{O}$ be the "lab" frame with coordinates (t, x^i) such that $\mathcal{O}$ is related to $\bar{\mathcal{O}}$ via a Lorentz boost along the $\hat{\mathbf{v}} = (\hat{v}_x, \hat{v}_y, \hat{v}_z)$ direction: in the $\mathcal{O}$ frame the black hole moves in the $\hat{\mathbf{v}}$ direction with boost velocity, v ($\delta_{ij}\hat{v}^i\hat{v}^j = 1$). As usual, we define $\gamma = 1/\sqrt{1-v^2}$. $H(\bar{x_\mu})$ and $\bar{l_\mu}$ (where a bar denotes $\bar{\mathcal{O}}$ frame) now transform as

$$H(x_\mu) = H(\bar{\Lambda}^{\bar{\nu}}_{\mu} \bar{x}_{\bar{\nu}}) \tag{19}$$

and

$$l_\mu = \bar{\Lambda}^{\bar{\nu}}_{\mu} \bar{l}_{\bar{\nu}}(\bar{\Lambda}^{\bar{\sigma}}_{\gamma} \bar{x}_{\bar{\sigma}}). \tag{20}$$

As stated previously, these transformations preserve the form of Eq. (10).

3+1 decomposition

The standard Arnowitt-Deser-Misner (ADM) $3+1$ form of the spacetime metric is given by

$$ds^2 = -\alpha^2 dt^2 + \gamma_{ij}(dx^i + \beta^i dt)(dx^j + \beta^j dt). \tag{21}$$

If we compare Eq. (10) to Eq. (21) and use the property that $l^\mu l_\mu = 0$, we find that the lapse is given by

$$\alpha = \frac{1}{\sqrt{1+2Hl_t^2}}, \tag{22}$$

and the shift is given by

$$\beta_i = 2Hl_t l_i \tag{23}$$

or

$$\beta^i = 2Hl_t \delta^{ij} l_j / (1+2Hl_t^2). \tag{24}$$

The 3-metric is

$$\gamma_{ij} = \eta_{ij} + 2Hl_i l_j \tag{25}$$

and the extrinsic curvature is determined from

$$K_{ij} = -\partial_t \gamma_{ij}/2\alpha + D_i\beta_j + D_j\beta_i \tag{26}$$

$$= -\partial_t(Hl_i l_j)/\alpha + 2[D_i(Hl_t l_j) + D_j(Hl_t l_i)] \tag{27}$$

and

$$\gamma^{ij} = \delta^{ij} - 2H\delta^{il}\delta^{jk} l_l l_k / (1+2Hl_t^2). \tag{28}$$

Note that

$$\det \gamma_{ij} = 1 + 2Hl_t^2. \tag{29}$$

To obtain explicit expressions for the 3-metric and extrinsic curvature we simply substitute Eqs. (11) and (12) [or Eqs. (15) and (16) for the case of Schwarzschild], along with Eq. (22), into Eqs. (25) and (27).

IV. RESULTS

In the discussion that follows we present results from tests done with the locator using the metric data discussed in the preceding section. We set up a 3-dimensional Cartesian grid, $\hat{\Sigma}$, of n^3 points on which we define a coordinate system. The black hole (either Kerr or Schwarzschild) is placed at the origin of this coordinate system. Using Eq. (25) and Eq. (27) we compute γ_{ij} and K_{ij} at each grid point except in the region that contains the curvature singularity of the black hole (for Schwarzschild $x^2+y^2+z^2 = 0$ and for Kerr $\rho = \sqrt{x^2+y^2+z^2} \leqslant a$). That is, we explicitly excise the singularity from the computational grid.

With this setup we consider two groups of tests. The first uses Schwarzschild data to conduct some basic tests of the locator and to illustrate some of its properties. The second part of this section examines apparent horizons for boosted Schwarzschild and Kerr black holes and illustrates the locator's ability to locate extremely distorted apparent horizons. Specifically we consider (1) $v=0$, $a=0$ (unboosted Schwarzschild), (2) $v=0$, $a\neq 0$ (unboosted Kerr), (3) $v\neq 0$, $a=0$ (boosted Schwarzschild) and (4) $v\neq 0$, $a\neq 0$ (boosted Kerr). From this point forward we also work in units yielding unit black hole mass, i.e. in units such that $M=1$.

A. Tests with Eddington-Finkelstein metric data

In this section we discuss some basic tests of the apparent horizon locator including a demonstration that the solutions obtained are $O(h^2)$, where h is the mesh spacing of the Cartesian grid. We take $\hat{v}_x=0$, $\hat{v}_y=0$, $\hat{v}_z=0$ and $a=0$, which generates metric data for an unboosted Schwarschild black hole in ingoing Eddington-Finkelstein coordinates. Despite the simplicity of the setup, we note that all components of γ_{ij} and K_{ij} are non-zero. The latter property makes this a good initial model problem to work with, because the computation is fully exercised in an analytically tractable situation. As stated earlier, the apparent horizon is expected to be located at $r=2M$, and we conduct the tests with data (i.e. metric and extrinsic curvature components) specified analytically where required.

1. Residual evaluation and second order convergence

We place the black hole at the origin of the computational domain $(x=0,y=0,z=0)$. For the spherically symmetric line element currently under consideration the horizon equation becomes the algebraic equation,

$$F(r)=\frac{1-2M/r}{r\sqrt{1+2M/r}}=0. \tag{30}$$

As follows immediately from the above expression at $r=2M$ we have $F=0$. A useful test of the evaluation of the expansion of the outgoing normals $F(r)$ is to see if indeed the residual $\hat{F}[\hat{\rho}]$ is correctly evaluated to $O(h^2)$ as

$$\hat{F}=F+e_2h^2+\cdots, \tag{31}$$

where e_2h^2 is the leading order truncation error term. Given that the exact value is known for $\hat{F}[\hat{\rho}]$ we can approximately compute the leading order truncation error. We carry out a convergence test by evaluating $\hat{F}[\hat{\rho}]$ on a 2-sphere of $r=2M$ for a series of mesh sizes, $N_s=17,25,33,49,65,97,129$. We examined the behavior of $\log\|\hat{F}\|_2$ versus $\log N_s$, where N_s is the number of mesh points on one side of the $N_s\times N_s$ mesh. At $r=2M$ $\hat{F}\sim e_2h^2$ and so the L_2 norm, $\|\hat{F}\|_2\sim\|e_2\|_2h^2$. Since $h\propto 1/N_s$ we expect that if the residual is $O(h^2)$ then the slope of a plot of $\log\|\hat{F}\|_2$ versus $\log N_s$ should be -2.0, which we validated via a least squares fit. A closely related test is to also evaluate $\log\|\hat{\rho}-\rho\|_2$ versus $\log N_s$, where $\hat{\rho}$ is the numerical solution from the apparent horizon locator and ρ is the exact horizon location. Figure 1 shows the result. From a least squares fit to a straight line, the slope is found to be about -2.1 which again validates our solution as $O(h^2)$.

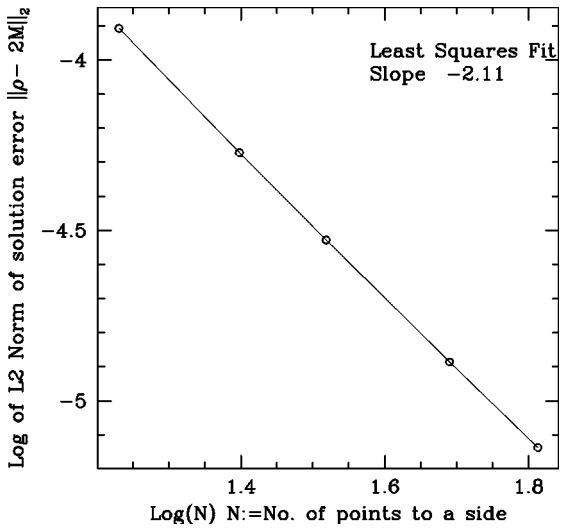

FIG. 1. This graph shows the logarithm of the error norm of the numerical solution, $\|\hat{\rho}-\rho\|_2$ versus $\log(N_s)$. Note that $M=1$. The slope of the graph is -2.1 and hence we conclude that the solution is $O(h^2)$.

2. Jacobian

For the 2D mesh (using $N_s=33$) discussed above, we generate the Jacobian matrix for a single Newton step. There are $N=1025$ *independent* points on $\hat{S}$ and hence $J_{\overline{\mu\nu}}$ is a 1025×1025 matrix. There are seven non-zero bands in this matrix with two additional ones in the vicinity of the poles at $\overline{\mu}=1$ and $\overline{\mu}=1025$. The structure reflects the domain of dependence of the finite difference operators used in the evaluation of $\hat{F}$. Here it comes from a combination of interpolations and finite differencing in the Cartesian mesh. Near $\overline{\mu}=1$ and $\overline{\mu}=1025$ the additional bands come from our special choice of interpolation stencils at the poles, as discussed in the Appendix.

The structure reflects the fact that a perturbation at a single mesh point affects the residual in a small neighborhood around it so we can optimize the generation of the Jacobian to $O(N)$ by evaluating $\hat{F}[\rho+\delta\rho]$ only in a small neighborhood of the perturbed point. In practice, the Jacobian generation was found to be order $O(N^p)$ where $p\approx 1.1$.

A matrix A is defined to be diagonally dominant [16] if its elements, A_{ij}, satisfy

$$\sum_{\substack{j=1\\ j\neq i}}^{n}|A_{ij}|\leqslant|A_{ii}|\text{for all } i. \tag{32}$$

TABLE I. This table summarizes results from a test of our apparent horizon (AH) locator's ability to find the AH in Schwarzschild data, starting from various initial conditions. In each case the initial surface is a 2-sphere of radius r_0. The number of iterations taken for the solution to achieve $\|\delta\rho\|_2 < 10^{-10}$ is listed in the second column. Note that the final error in the solution remains a constant provided the solver is able to drive $\|\delta\rho\|_2$ below the specified stopping criterion. The perturbation parameter used to generate the Jacobian was 10^{-5}.

r_0	No. iterations	Final $\|\hat{F}\|_2$	$\|\hat{\rho}-\rho\|_2$	% error
0.5	10	2.2×10^{-10}	3.0×10^{-5}	1.5×10^{-3}
0.75	9	2.5×10^{-10}	3.0×10^{-5}	1.5×10^{-3}
1.00	9	9.7×10^{-11}	3.0×10^{-5}	1.5×10^{-3}
1.25	8	9.5×10^{-11}	3.0×10^{-5}	1.5×10^{-3}
1.50	7	1.6×10^{-10}	3.0×10^{-5}	1.5×10^{-3}
1.75	7	9.6×10^{-11}	3.0×10^{-5}	1.5×10^{-3}
2.00	4	9.7×10^{-11}	3.0×10^{-5}	1.5×10^{-3}
2.25	7	9.8×10^{-11}	3.0×10^{-5}	1.5×10^{-3}
2.50	8	1.0×10^{-10}	3.0×10^{-5}	1.5×10^{-3}
2.75	9	9.5×10^{-11}	3.0×10^{-5}	1.5×10^{-3}
3.00	12	9.9×10^{-11}	3.0×10^{-5}	1.5×10^{-3}

We found that our Jacobians were *not* diagonally dominant in general.

This is of interest since for some iterative solution techniques (Gauss-Seidel and SOR, for example) a sufficient condition for the solution of a linear system, $A\cdot x=b$, is that the matrix, A, be diagonally dominant. In our case we concluded from early experiments that indeed such simple iterative solvers did not converge for this problem.

Additionally, the Jacobian matrix is generally not symmetric but it *is* well conditioned for the spacetimes that we have considered. For a 33×33 run the Jacobian has a condition number, κ, of about 10^4 to 10^5 where κ is defined by

$$\kappa=\|A\|\|A^{-1}\|. \tag{33}$$

The condition number tells us how close the matrix A is to being ''numerically singular.'' A very large condition number or a reciprocal condition number close to machine epsilon tells us that A is effectively singular. An identity matrix has a condition number of 1. To estimate κ we used the LINPACK library routine, DGECO [17]. For completeness we note that in their definition of the condition number, Dongarra *et al.* [17] use the L_1 norm.

3. Solution of the linear system

As stated before, to locate the apparent horizon using our technique, we have to obtain a solution, $\delta\hat{\rho}$, to the linear system

$$\hat{J}\cdot\delta\hat{\rho}=-\hat{F}[\hat{\rho}]$$

which is the discrete form of Eq. (8).

Since the properties of the matrix preclude the use of iterative methods such as SOR (not to mention that such methods are not very efficient), we use a modified conjugate-gradient method due to Kershaw [18]. (The standard form of the conjugate gradient method will not work since J is not symmetric.) Kershaw's method, termed the incomplete LU-conjugate gradient method (ILUCG), can solve any linear system, $A\cdot x=b$, with A a nonsingular, generally sparse matrix. The method involves preconditioning the matrix via an incomplete LU decomposition. This method has worked quite well for our purposes, although in principle other linear solvers could certainly be used.

4. Solution for the apparent horizon location

As a first test of our approach we carried out a basic test of the Newton solver's ability to locate apparent horizons in Eddington-Finkelstein data. The test involved searching for a solution using a set of different initial starting 2-spheres (parametrized by their radius, r_0) and examining the final solution error and convergence properties. Table I shows the error and residual for $r_0=0.5,\ldots,3.0$, $N_s=33$ and stopping criteria of $\|\delta\hat{\rho}\|\sim10^{-10}$. For each of the cases, once within the basin of attraction, the solver converged quadratically to the finite difference solution, as is to be expected for a global Newton iteration.

As mentioned in the table caption, for this test we used a perturbation parameter, $\epsilon=10^{-5}$. We found empirically that for this problem, an optimum value of ϵ was between 10^{-4} and 10^{-6}. In general, ϵ must be chosen large enough such that $\hat{F}[\hat{\rho}+\epsilon]$ and $\hat{F}[\hat{\rho}]$ are sufficiently different to prevent a catastrophic loss of precision in the calculation of the Jacobian. A contrasting requirement is that one must choose ϵ small enough to produce a sufficiently accurate approximation of the Jacobian.

5. Numerical metric data

For the tests discussed thus far we have used data analytically computed at each point as needed. Since the ultimate goal is to incorporate this apparent horizon location algorithm into an evolution code, it is useful to gauge the performance of the algorithm with ''numerical'' metric data (i.e. tabulated data) and with the data structures expected in the real application, where, for instance, part of the domain is excised from consideration. Thus we set up the same Eddington-Finkelstein data on a 3D Cartesian grid of n^3

points, with a region of this grid excised to emulate the situation in an evolution code where the interior of the black hole is excluded. The apparent horizon surface which is embedded in this 3D Cartesian grid typically does not lie on Cartesian grid points and as a result an interpolation tool is required. If the surface mesh, during the course of the Newton iterations, overlaps the excised region then extrapolation is required. We make use of an interpolating routine written by Klasky [19] that can handle such situations. Using this interpolator tool we can obtain the 3-metric, extrinsic curvature and the spatial derivatives of the 3-metric at any point from a regularly spaced 3D array of values. Of course, the use of the interpolator brings in additional truncation errors associated with the interpolation or extrapolation operations. However, in the following we show that even with extrapolation errors, the solver works quite well in locating apparent horizons.

We excise the region of the 3D grid interior to a sphere of radius R_m centered at (x_m, y_m, z_m) so that the metric data is defined for $r > R_m$ and undefined for $r < R_m$. Here, r is the Cartesian distance in Kerr-Schild coordinates from the excision center.

In the following discussion on radial and offset apparent horizon locations we take $n = 65$ for the Cartesian grid (with $h = 1/8$) and $N_s = 33$ for the surface mesh. The stopping criterion used in the horizon finder is $\beta = 10^{-4}$. That is, if $\|\delta\rho\|_2 < \beta$ then the Newton iterations are stopped. The perturbation parameter, ϵ, is taken to be 10^{-4}. Interpolations are performed to $O(h^4)$. The initial guess surface used is a sphere of radius $r_0 = 2.1M$ centered at the origin of the Cartesian grid. With these parameters we carry out two set of tests. The first is a radial test of the horizon locator with the use of the interpolator, and the second is an offset test. These tests examine the effect of extrapolation of metric data on the evaluation of residual, $\hat{F}$, and on the solution of the apparent horizon equation.

6. Apparent horizon location (radial tests with excision)

In this test case we center the black hole at (0,0,0). The masked region is also centered at (0,0,0). We carry out a series of tests with the excision radius, R_m, varying from 1.5 to 2.6. Thus the apparent horizon is in the defined region ($R_m < 2M$) for some of the tests, and for others it is inside the excised region ($R_m > 2M$). This provides evidence of the effect of extrapolations on the residual of the apparent horizon equation, $\hat{F}$, and the error in its solution. Figure 2 illustrates the behavior of the L_2 norm of the residual, $\|\hat{F}\|_2$, as a function of R_m. Figure 3 shows the percentage relative error of the solution of the apparent horizon equation as a function of R_m. The percentage relative error is calculated using the exact solution for the location of the apparent horizon, $r = \rho(\theta,\phi) = \overline{\rho} = 2M$, as $e \equiv \|\rho - \overline{\rho}\|/\overline{\rho} \times 100\%$. For $R_m < 2M$ the interpolator uses interpolation for regions near the apparent horizon location ($r = 2M$), while for $R_m > 2M$ it uses extrapolation. As R_m increases beyond $2M$, the errors due to extrapolation increase, as expected. This can be seen in Fig. 2 where $\|\hat{F}\|_2$ increases quickly for $R_m \gtrsim 2.4$, as does the solution error *per se*, which is shown in Fig. 3. At $R_m = 2.5M$, the solver cannot drive $\|\delta\rho\|_2$ below 10^{-4}, and so fails to meet the stopping criterion. This can be understood in terms of the Cauchy-Schwarz inequality [16]. Since $\|J \cdot \delta\rho\|_2 = \|\hat{F}\|_2$ we have that

$$\|\delta\rho\|_2 \geqslant \frac{\|\hat{F}\|_2}{\|J\|_2}. \tag{34}$$

At $R_m = 2.2$ where $\|\hat{F}\|_2 \sim 10^{-3}$ and $\|\delta\rho\|_2 \sim 10^{-5}$, we have from Eq. (34) that $\|J\|_2 \sim 10^2$. Therefore at $R_m = 2.5M$ we expect with $\|\hat{F}\|_2 \sim 10^{-2}$ that $\|\delta\rho\|_2 \sim 10^{-4}$. By relaxing the criterion for $2.5\,M \leqslant R_m \leqslant 2.6\,M$ we can still obtain a solution. For $R_m > 2.6M$, the convergence progressively worsens. For example, at $R_m = 2.9$, $\|\hat{F}\|_2$ could not be brought below

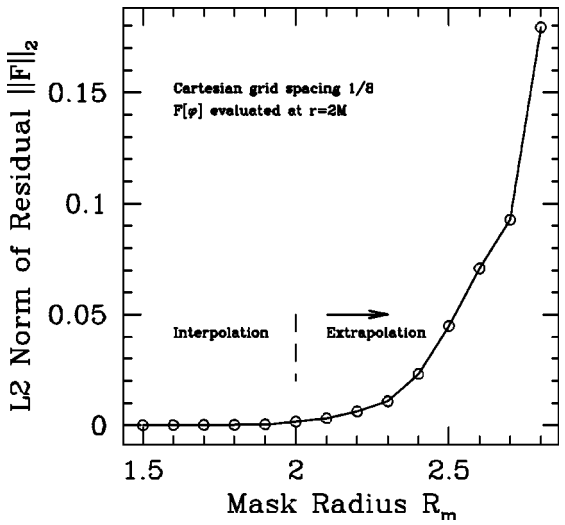

FIG. 2. Graph of the L_2 norms of the residual, $\|\hat{F}[\varphi]\|$, versus the mask radius, R_m.

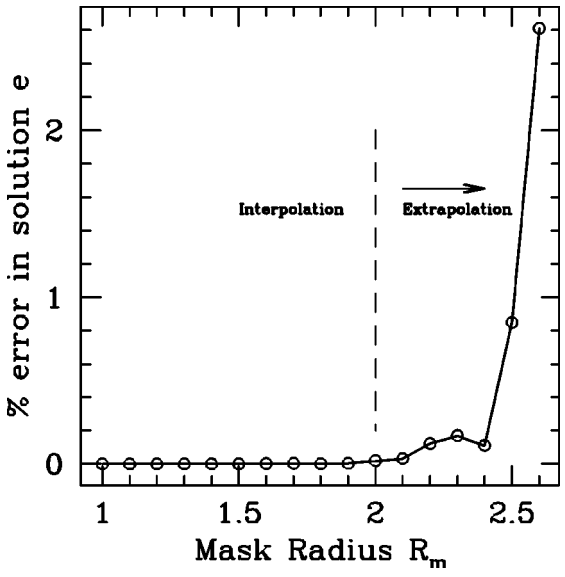

FIG. 3. Percentage relative error in ρ versus mask radius. Past $R_m > 2.5$ the Newton solver could not reduce $\|\hat{F}\|_2$ below 10^{-4}.

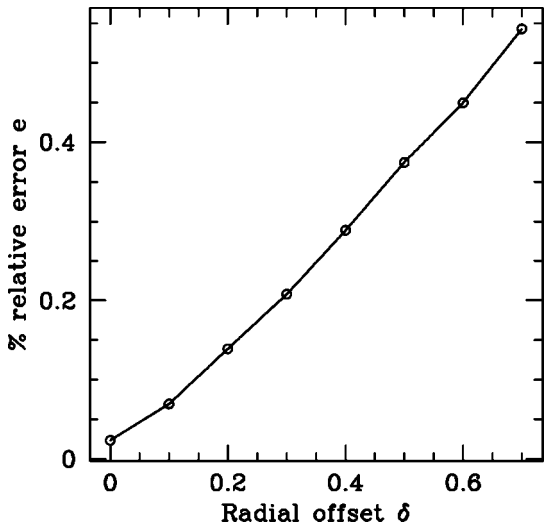

FIG. 4. Percentage relative error in the apparent horizon location as a function of the offset δ.

10^{-3}, and the solution error is 5%. The amount of error sustained from interpolation of the metric data is dependent on the resolution of the Cartesian grid and the behavior of the functions being interpolated. If the gradients of γ_{ij} and K_{ij} are large near the horizon then a larger interpolation error results. This in turn leads to a larger truncation error in $\hat{F}$. In the numerical evolution of black hole spacetimes with excision we conclude from this experiment that buffer zones may not be necessary for the location of apparent horizons. However, in an evolutionary context, buffer zones might be necessary for other reasons.

7. Locating offset apparent horizons

We now consider a situation where we have an ''offset'' black hole such that the apparent horizon overlaps the excised region. This is an important case to consider because it is relevant for the tracking of moving black holes [20].

The center of the masked region is at $(0,0,0)$ and the black hole of radius $2M$ is centered at $(\delta/\sqrt{3},\delta/\sqrt{3},\delta/\sqrt{3})$, so that the radial distance between the mask center and the hole is δ. With a grid spacing of $h=1/8$, an offset of $\delta=1$ thus corresponds to approximately 8 grid zones. Figure 4 shows the percentage relative error in the apparent horizon location as a function of the offset δ. As the graph illustrates, up to $\delta=0.7$ the percentage relative error is below 1%. (At $\delta=0.7$ the percentage error is 0.6%.) From $\delta=0.7$ onwards, however, the solver becomes sensitive to initial conditions and extrapolation errors, and quickly ceases to converge.

At $\delta=0.7$, about 5–6 grid points offset, we are still able to find horizons. Generally, in explicit time-evolution codes the Courant-Friedrich-Levy (CFL) condition [21] restricts the black hole motion from one time slice to another, to be less than one zone ($\delta<h$ or about $\delta\sim 0.1$ in our test case). Hence we expect, based on the results for our model spacetime as shown in Fig. 4, that in such an evolutionary scheme with a similar resolution we will be able to locate black hole apparent horizons to a precision of order 0.1%.

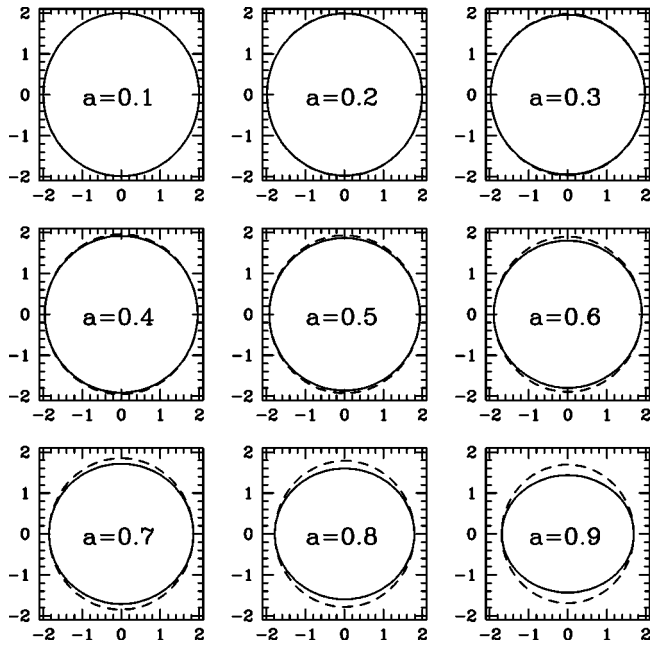

FIG. 5. $\theta=\pi/2$ and $\phi=\pi$ cross sections of apparent horizons located are shown for various values of a. The solid line shows the $\phi=\pi$ slice of the apparent horizon. The dashed line shows the $\theta=\pi/2$ slice of the horizon. As expected the $\phi=\pi$ slices show increasing deformation for increasing a.

B. Apparent horizons in Kerr data

In this section we focus on the apparent horizon location in Kerr, boosted Schwarzschild, and boosted Kerr spacetimes. We begin with the Kerr case, where we excise a 2-sphere of radius $r>a$ centered about the origin from the computational domain to avoid the ring singularity structure of the Kerr black hole. Using the apparent horizon locator, we find horizons for various values of the angular momentum parameter: $a=0.0,0.1,0.2,\ldots,0.9$. In each case, the locator begins with a trial surface that is a 2-sphere of radius $r_0=2M$ and we use $N_s=33$, $\epsilon=10^{-5}$ and $\beta=10^{-11}$. Figure 5 shows a cross section of the computed horizon in the xz plane as a function of a. For non-zero a the apparent horizon apparently has the shape of an oblate spheroid.

In order to perform a convergence test we carried out a series of runs with $a=0.9$ and $N_s=17,25,33,49,65$. We found that the error in the solution, $\|(\hat{r}-r_+)/r_+\|_2$, was $O(h^2)$. Here r_+ is given by Eq. (17), and $\hat{r}$ is computed from the discrete form of Eq. (14).

We compute the area of the apparent horizon by projecting γ_{ij} onto the 2D mesh to obtain an area element $\sqrt{^{(2)}\gamma}\,d\theta\,d\phi$. We integrate this element over the discrete 2-surface, $\hat{\mathcal{S}}$, to obtain the numerically computed area, $\hat{\mathcal{A}}$. Figure 6 shows the percentage errors in the area as a function of mesh size.

We now consider Schwarzschild and Kerr black holes boosted in the yz direction. Specifically, we take $\hat{v}_x=0,\hat{v}_y=1/\sqrt{2}\,v,\hat{v}_z=1/\sqrt{2}\,v$ and $a=0$ or $a=0.9$. For both values of a, we locate apparent horizons for $v=0,0.1,\ldots,0.9$. From $0\leqslant v\leqslant 0.8$, we started with a two-sphere of radius $2M$

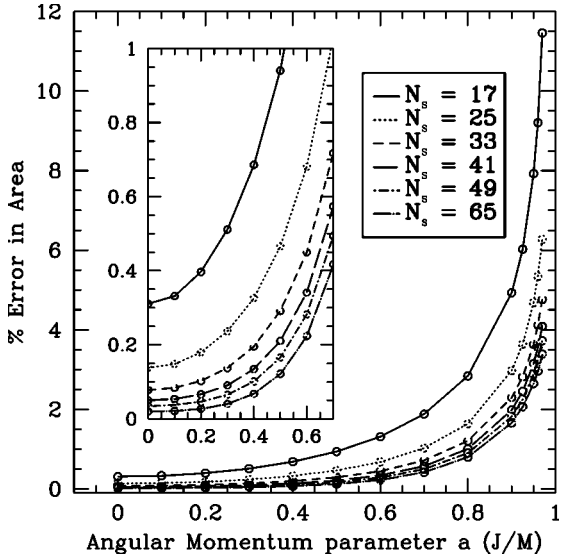

FIG. 6. The percentage error in the area of the apparent horizon for a Kerr hole versus a is shown for $N_s=17,25,33,41,49,65$.

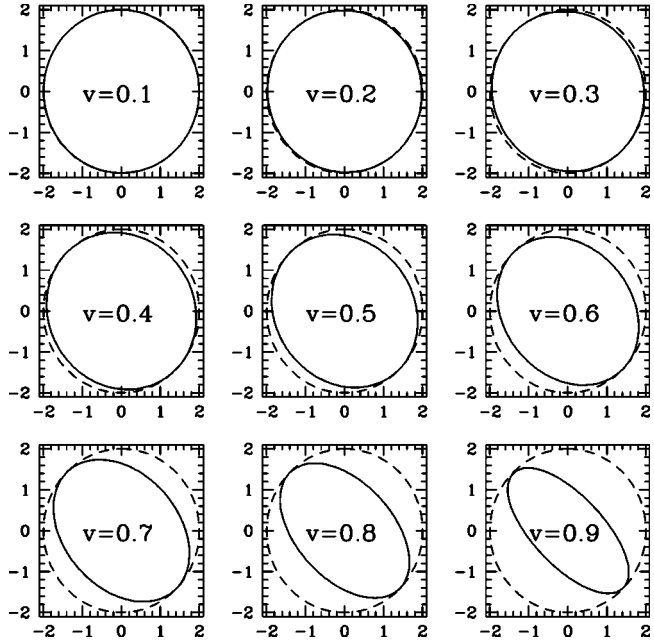

FIG. 7. This series of plots shows y-z cross sections of a Schwarzschild black hole apparent horizon located for boost velocities of $v=0.0,0.1,\ldots,0.9$ in the y-z direction. The dashed circle in each of these figures is the apparent horizon for an unboosted Schwarzschild black hole. Note that the points of contact of the dashed and solid curves lie along a line in the yz plane which is orthogonal to the direction of the boost.

and found an apparent horizon with outgoing expansions driven down to 10^{-12}. For $v>0.8$ we had difficulty achieving this convergence criterion. As a result we utilized the solution at $v=0.8$ as an initial guess and were subsequently able to find horizons by stepping every 0.25 from $v=0.8$ to $v=0.9$. For these runs, we again used $\epsilon=10^{-5}$. At $v=0$ the initial guess *is* the apparent horizon, and, in this case, the expansions were driven to $\sim 10^{-12}$ within six Newton iterations. The first Newton iteration took the expansions to $\sim 10^{-6}$. For $v=0.5$ starting from an initial guess of a sphere of radius $\rho=2M$, it took four Newton iterations to drive the expansions to $\sim 10^{-6}$ and nine Newton iterations to get down to $\sim 10^{-12}$. Typically, in a numerical time evolution of such a spacetime we would not need to drive the expansions down to this level. In particular, if we are utilizing a surface *within* the apparent horizon as an excision boundary then we need only to drive the expansions down far enough to be certain an apparent horizon *is* present outside of $\hat{\mathcal{S}}$. Figure 7 shows the yz cross section of the apparent horizon for various boost velocities compared with an unboosted black hole apparent horizon cross section. We find that the apparent horizon is Lorentz contracted in the yz direction in the boosted coordinates. This is consistent with the slicing that we have chosen where the event horizon appears Lorentz contracted. We know that in these spacetimes the apparent horizon coincides with the event horizon and we find that this is indeed the case. First, the area of the apparent horizon coincides with the area of the event horizon which is invariant under a boost. Figure 8 shows the error in the apparent horizon area as a function of v for various resolutions. We find that with increasing resolution the error in the area converges towards zero. This demonstrates that the area of the apparent horizon found *is* approximately invariant under a boost. Additional evidence is provided by Fig. 9 where we show the error in the radial coordinate, $r=2M$, on the apparent horizon for various boost velocities. In this case the black hole is boosted in the xyz direction for generality. That is, $\hat{v}_x=1/\sqrt{3},\hat{v}_y=1/\sqrt{3},\hat{v}_z=1/\sqrt{3}$ and $a=0$. Here $r=\sqrt{x^2+y^2+z^2}$ is computed using the boosted coordinates, $x^\mu=\Lambda^\mu_{\ \nu}\overline{x^\nu}$, where $\overline{x^\nu}$ are the unboosted coordinates.

Figure 10 shows surface plots of the apparent horizon for $v=0,0.3,0.6$ and 0.9 displayed in Kerr-Schild Cartesian coordinates. Note how distorted the apparent horizon gets with increasing boost velocities. As also seen in the figures for the

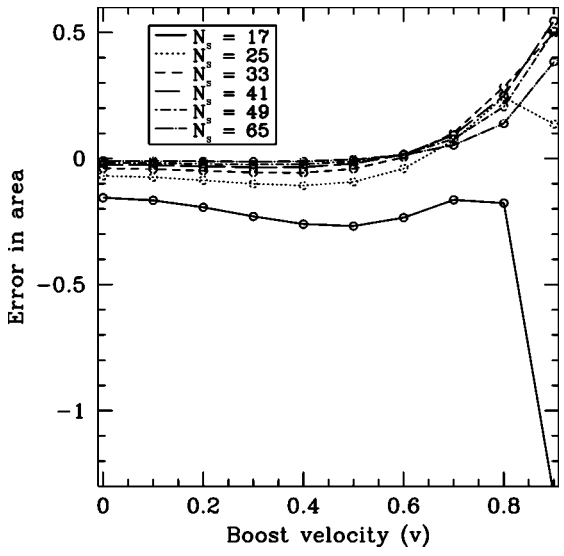

FIG. 8. Error in the areas of apparent horizons, $\|\hat{\mathcal{A}}-\mathcal{A}\|_2$, found for a Schwarzschild black hole boosted in the y-z direction.

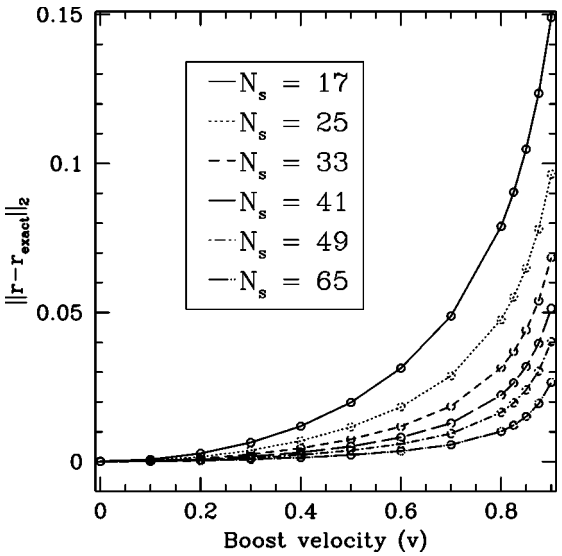

FIG. 9. Error in the radial coordinate, r where $r_{exact}=2M$ for a Schwarzschild black hole apparent horizon for $v=0.0,\ldots,0.9$. The black hole is boosted in the xyz direction.

yz boosts, the boosted apparent horizons in this generic case are always contained within the apparent horizon for $v=0$. That is, the boost contracts the apparent horizon in the boost direction. Again for a boost velocity of $v=0.5$ it took the solver eight Newton steps to drive the expansions to the stopping criterion $\beta=10^{-12}$. On average it took four Newton steps to drive the expansions to $\sim 10^{-6}$ and nine Newton steps to $\sim 10^{-12}$, starting from an expansion of 0.1.

For the case of a boosted Kerr black hole with $a=0.9$, the results are very similar to those of the Schwarzschild black hole just discussed. Note that in this case, with $a=0.9$ and $v\rightarrow 0.9$, the apparent horizons are even more distorted (nonspherical). These results show that our algorithm for finding apparent horizons does quite well with such large distortions. In addition the cost of finding these surfaces increases by only two additional Newton steps. Figure 11 shows the yz cross sections for the apparent horizon found for $a=0.9$ as a function of v. Again the boosted apparent horizon is contained within the unboosted one and Lorentz contracted. Figure 12 shows the error in the area for the same data. With $a=0.9$ we expect that the area should be ~ 36. The graph shows that for increasing resolution the error in the area tends towards zero. Hence the area remains fixed with increased boost velocity as expected.

Similarly, the error in r [computed from Eq. (14) using boosted coordinates] tends to zero with increasing resolution as shown by Fig. 13. The apparent horizons found here were obtained with $\hat{v}_x=1/\sqrt{3},\hat{v}_y=1/\sqrt{3},\hat{v}_z=1/\sqrt{3}$ and $a=0.9$. That is, the boost was in the xyz direction with magnitude v. Again we find that r on the apparent horizon converges to $r_+\sim 1.4$ with increasing resolution for all boost velocities. At a resolution of 33×33 we find about 8% error, and 1% at 65×65. Figure 14 shows surface plots of the apparent horizon for the boosted Kerr black hole for $v=0,0.3,0.6$ and 0.9. For $v=0$, our algorithm required one less Newton step to drive the expansions down to 10^{-12} than it did for $v=0.9$. In

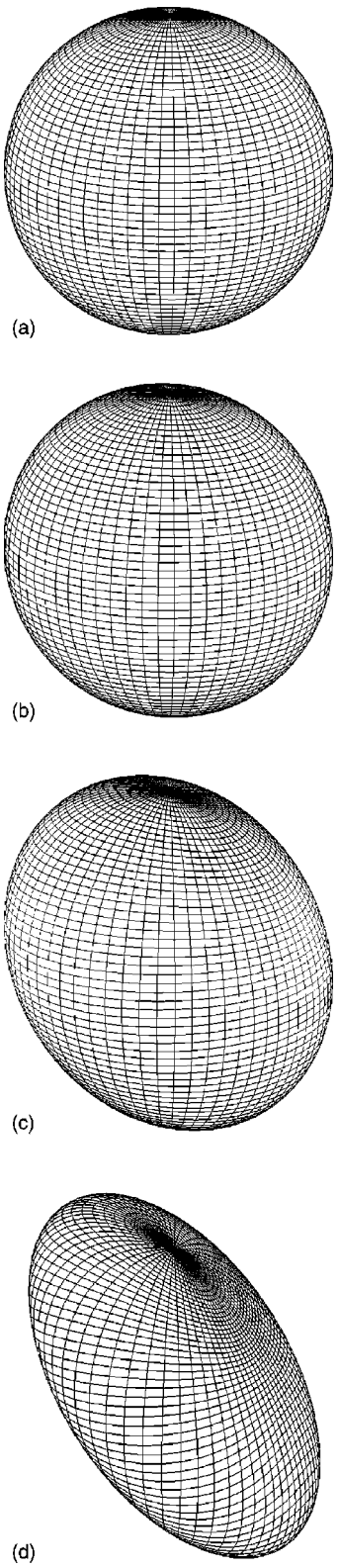

FIG. 10. Plots of the apparent horizon for the $a=0.0$ runs for $v=0.0,0.3,0.6$ and 0.9 (left to right, top to bottom) for boosts in the xyz direction. The mesh used to find the apparent horizon is shown from a top perspective. As the boost velocity is increased we see that the surface is contracted in the xyz direction.

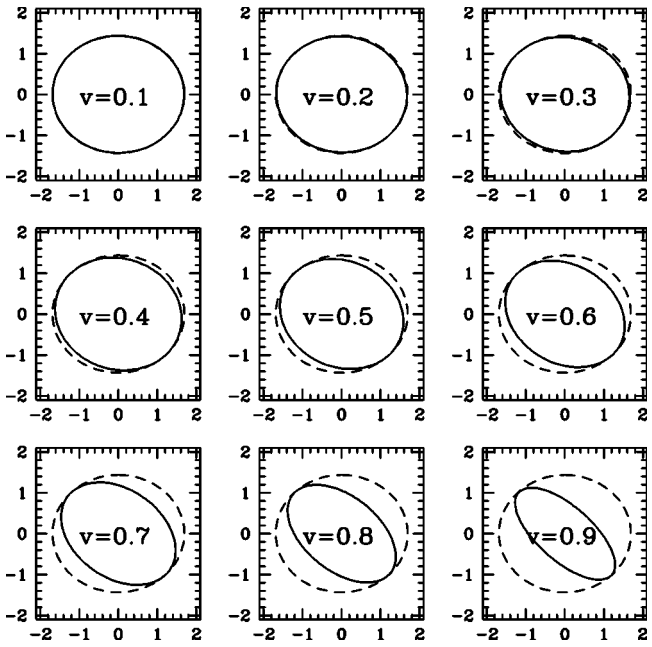

FIG. 11. The y-z cross section of Kerr ($a=0.9$) black hole apparent horizons located for boost velocities of $v=0.0,0.1,\ldots,0.9$ in the y-z direction. The dashed circle in each of these figures is the apparent horizon for an unboosted Schwarzschild black hole. As in Fig. 8, note that the points of contact of the curves lie along a line in the yz plane which is orthogonal to the direction of the boost.

both instances, it took six Newton iterations to drive the expansion from about 0.2 at the inital step to 10^{-6}. Hence, this algorithm has the advantage that given sufficient resolution on the computational mesh, the work done does not drastically increase for increasing distortions.

V. COMPUTATIONAL EFFICIENCY

Our algorithm is dominated primarily by computations of the Jacobian matrix in the use of Newton's method. As discussed above, these operations are optimized such that they scale as approximately $\mathcal{O}(N)$, where N is the total number of points on the two-dimensional solution mesh. The time taken per Newton iteration is independent of the distortion of the apparent horizon. However, the number of Newton iteration steps is determined by the ''distance'' of the initial starting surface from the final solution. During the course of an evolution it is expected that the apparent horizons over several time slices will be ''close'' enough to each other that two to three Newton iterations will be sufficient to locate the horizon at low accuracy with the expansion of the outgoing null rays on its surface being at the level of 10^{-5} or 10^{-6}. Obtaining better accuracy requires more Newton iterations, and the convergence rate also depends on the accuracy of the background metric data. Typically in our model problems, eight iterations drive the residuals below 10^{-10}.

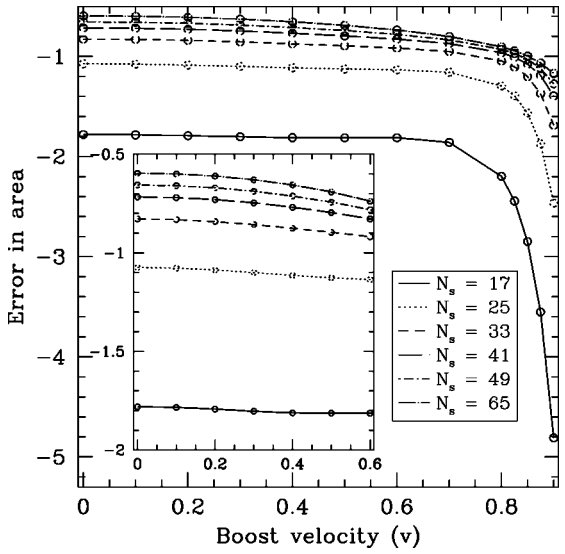

FIG. 12. The error in the areas of apparent horizons found for a Kerr black hole boosted in the y-z direction with $a=0.9$.

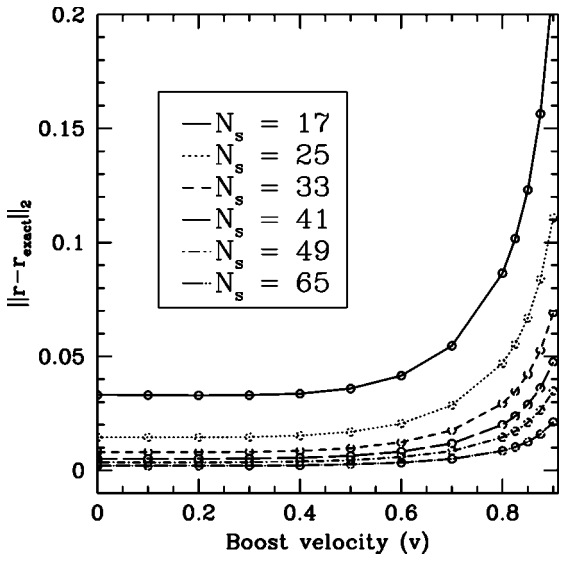

FIG. 13. This figure shows the error in the spheriodal radial coordinate location for a Kerr black hole apparent horizon ($a=0.9$) for $v=0.0,\ldots,0.9$. The black hole is boosted in the xyz direction.

One of the drawbacks of a Newton method for finding apparent horizons is its sensitivity to the initial guess. An initial guess outside of the radius of convergence will not lead to a solution. Additionally, Newton methods are known to be sensitive to high frequency components in the solution. This has been demonstrated in an axisymmetric context by Thornburg [8]. Sensitivity to the initial guess can be easily handled by combining the Newton method algorithm with apparent horizon trackers that are based on flow methods. The flow finder is used to obtain an initial guess for the Newton method which then converges on the solution very quickly.

The efficiency of our method can be compared to the efficiency of other approaches (variations of flow methods) due to Tod, as developed by Shoemaker *et al.* [12] and fast flow methods developed by Gundlach [13]. The flow method is based on a parabolic partial differential equation whose rate of convergence to the solution slows as the solution is approached. Typically for a 33×33 run the flow method takes hundreds of times longer than our method to converge

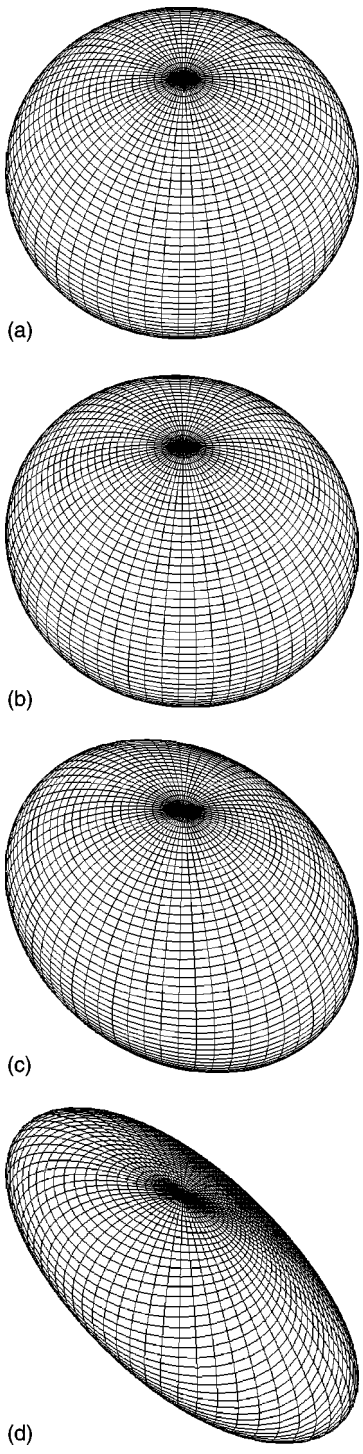

FIG. 14. This figure shows plots of the apparent horizon for the $a=0.9$ runs for $v=0.0,0.3,0.6$ and 0.9 for boosts in the xyz direction. The mesh used to find the apparent horizon is shown from a top perspective. As the boost velocity is increased we see that the surface is contracted in the xyz direction.

down to expansions of 10^{-4}. The advantage of the flow method, however, is its ability to find multiple apparent horizons from an arbitrary initial guess. A hybrid flow or direct-Newton solver should thus result in a robust apparent horizon finding scheme.

We can also compare our implementation to spectral decomposition methods. We concentrate on a method similar to that of Nakamura *et al.* [4] in which the equation for the apparent horizon surface is written

$$\rho(\theta,\phi)=\sum_{l=0}^{l_{\max}}\sum_{m=-l}^{l} a_{lm}Y_{lm}(\theta,\phi). \tag{35}$$

We do not have access to an apparent horizon finder based on pseudo-spectral methods but we will analytically compute the coefficients for the case of a boosted Schwarschild black hole; this will give some insight into the range of harmonics required, and some idea of what scaling of these methods might be.

In Kerr-Schild coordinates, the hole, with a boost in the z direction, has the shape of a spheroid,

$$\frac{x^2}{a^2}+\frac{z^2}{b^2}=1, \tag{36}$$

where we have suppressed the y direction.

Notice that the axes a,b of the ellipsoid obey $b^2/a^2=1-v^2$, which demonstrates that the eccentricity is equal to the boost velocity, $\epsilon=v$, for this case. Hence even ellipses with a moderate ratio of axes, such as that for $v=0.9$, where the ratio is a little less than 0.5, have moderately large eccentricities. We will approximate the form Eq. (36) with an axisymmetric series of the form Eq. (35) (the general case of locating an apparent horizon would have nonaxisymmetric terms also). We find it more convenient to work with Legendre polynomials than with the spherical harmonics directly.

Since we work with Legendre polynomials, we drop the ϕ dependence in the spheroid expression, to obtain

$$R(\theta)=b/\sqrt{1-\epsilon^2\sin^2\theta} \tag{37}$$

$$=b/\sqrt{1-\epsilon^2(1-q^2)}, \tag{38}$$

where $q=\cos\theta$.

To obtain the expansion of expression Eq. (38) in terms of P_m, we first expand using the binomial theorem,

$$R(\theta)/b=\sum_{s=0}^{\infty}\binom{-1/2}{s}(-1)^s\epsilon^{2s}(1-q^2)^s. \tag{39}$$

This converges for all $v<1$.

Using the binomial theorem again for $(1-q^2)^s$ we substitute

$$(1-q^2)^s=\sum_{r=0}^{s}\binom{s}{r}(-1)^r q^{2r} \tag{40}$$

in Eq. (39) to obtain

$$R(\theta)/b=\sum_{s=0}^{\infty}\binom{-1/2}{s}(-1)^s\epsilon^{2s}\sum_{r=0}^{s}\binom{s}{r}(-1)^r a_{sr} \tag{41}$$

where

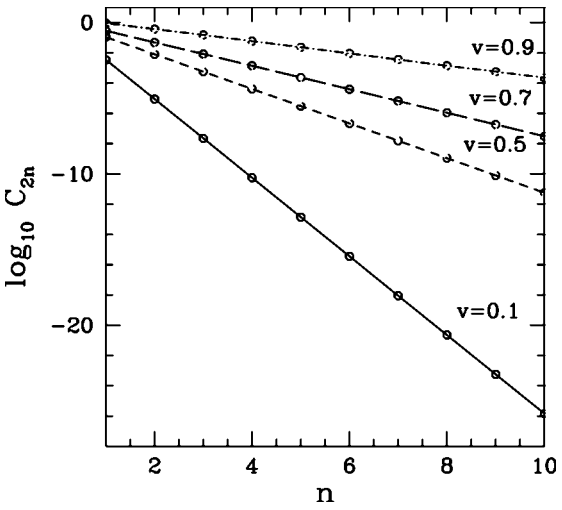

FIG. 15. $\log_{10}(C_{2n})$ for $n=1$ to 10 are shown for $v=0.1$, $v=0.5$, $v=0.7$ and $v=0.9$. The coefficients scale as e^{-kn} where k is determined by the shape of the horizon. For $v=0.1$ we have $k\sim 6$ and for $v=0.9$ $k\sim 0.9$.

$$a_{sr}(q)=\sum_{n=0}^{r}\frac{2^{2n}(4n+1)(2r)!(r+n)!}{(2r+2n+1)!(r-n)!}P_{2n}(q) \qquad (42)$$

and we made the substitution

$$q^{2r}=\sum_{n=0}^{r}\frac{2^{2n}(4n+1)(2r)!(r+n)!}{(2r+2n+1)!(r-n)!}P_{2n}(q).$$

By exchanging the summations over r and n and then n and s it is possible to rewrite Eq. (41) as

$$r(\theta)=\sum_{n=0}^{\infty}C_{2n}P_{2n}(\theta), \qquad (43)$$

where

$$C_{2n}=2^{2n}(4n+1)\sum_{s=n}^{\infty}\binom{-1/2}{s}(-1)^s\epsilon^{2s}$$
$$\times\sum_{r=n}^{s}\binom{s}{r}\frac{(-1)^r(2r)!(r+n)!}{(2r+2n+1)!(r-n)!}. \qquad (44)$$

Figure 15 gives the coefficients C_{2n} for $n=1,\ldots,10$, and for several values of v. While Fig. 15 shows the exponential convergence of algorithm with n, it also shows that the coefficient of the convergence is small for $v\sim 0.9$. It can be seen that the number of required terms approaches 20 for $v=0.9$ if the error is required to be less than 10^{-3}. (The general sum would have polynomials of odd as well as even order, and for each l, a set of azimuthal quantum numbers spanning $-2n$ to $2n$.) Hence in general, to compute the distorted apparent horizon would take a search over 20^2 parameters in a minimization routine. This is equivalent to inverting a full matrix of this size, and would be expected to be slow. The elliptic PDE solver is expected to be much faster.

VI. DISCUSSION

We have demonstrated in this paper that our method based on finite difference techniques is viable for locating very distorted boosted Kerr black hole apparent horizons. We have shown that the located horizons obey the expected analytical rule of invariance of the area of the event horizon, in cases corresponding to at-rest or boosted single black holes, where the apparent horizon is known to coincide with the event horizon. We have additionally given a number of computational tests demonstrating the behavior of the locator on interpolated or extrapolated data which are similar to realistic data obtained from evolutions. In other contexts the algorithm has been thoroughly tested with a canonical set of test problems such as two- and three-black-hole initial data sets. Additionally, it has been successfully used to track apparent horizons in the evolution of geodesically sliced Schwarzschild black hole data [22,23], as well as in the evolution of boosted Schwarzschild data [20]. Those tests and the tests given here show its viability as a method for locating black hole apparent horizons and using them for black hole excision. Since black hole excision would appear to be vital for long-term evolutions of single or multiple black hole spacetimes, it is very useful to have efficient apparent horizon locators that can locate apparent horizons quickly, relative to the time taken for an evolution time step.

It is a fact that our method as currently implemented can find only a *single, isolated* apparent horizon. Thus, its speed is counteracted by the impossibility of its use in generic 2-hole cases. However, it may be possible to use a flow method which would recognize the existence of separate black holes, and roughly locate the two holes to some accuracy. These approximate solutions (2-surfaces) could then be used as initial conditions for the current algorithm, which should then quickly converge to a highly accurate result. We are confident that a tool based on the combination of the two methods would be of great utility.

ACKNOWLEDGMENTS

This work was supported by NSF PHY9407194, PHY9722068, PHY9800722, PHY9800725, PHY9800970 and by NSERC. We wish to thank S. Klasky for providing and developing the 3D interpolation tools used in a part of this work as well as for discussions and work on applications of interpolation with excision. M.F.H. wishes to thank J. Thornburg for stimulating discussions on apparent horizon location during the early part of this work. We also gratefully acknowledge the hospitality of the Institute for Theoretical Physics, UCSB, where part of this work was carried out.

APPENDIX: EVALUATION OF THE RESIDUAL

The evaluation of Cartesian derivatives on $\hat{\mathcal{S}}$ is carried out by constructing 3D finite difference stencils at each mesh point on $\hat{\mathcal{S}}$. The finite difference stencil, denoted by $\mathcal{N}$, consists of 26 additional points around each mesh point. These 26 points are $\pm\delta x$, $\pm\delta y$ and $\pm\delta z$ away from the central mesh point. These points, as shown, are organized into three

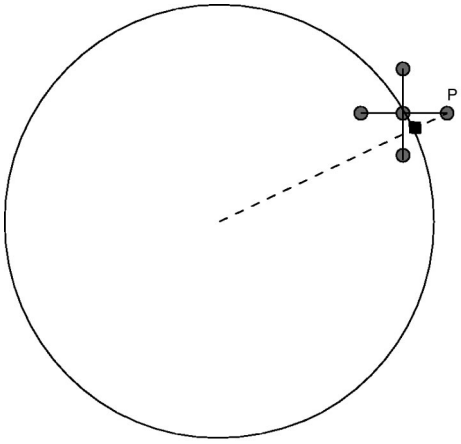

FIG. 16. P is the point at which we wish to estimate φ. The dashed line is the radial line from the origin of our spherical coordinate system to P. The filled square on the surface is the interpolation point where we evaluate $\rho(\theta_x,\phi_x)$.

planes of constant z: $z=z_0-\delta z, z_0, z_0+\delta z$. Each plane contains nine nearest neighbors of the center point, including the center point itself in the case of $z=z_0$. We use a single discretization scale h ($\delta x=\delta y=\delta z=h$) which is always proportional to the mesh spacing $\delta\theta=\pi/(N_s-1)$.

To define $\varphi(x,y,z)$ at each stencil point $\mathbf{x}\in\mathcal{N}$ we use its split into radial and angular parts, $\varphi(x,y,z)=r-\rho(\theta,\phi)$. For each stencil point $\mathbf{x}$ we compute the corresponding spherical coordinates (r_x,θ_x,ϕ_x). This point can be thought of as a ray emanating from the origin of our spherical coordinate system (which coincides with the origin of our Cartesian coordinate system) along (θ_x,ϕ_x) of length r_x. Figure 16 labels the point $\mathbf{x}$ as P. The dashed line from P to the origin is the ray from the origin. Its intersection with $\hat{\mathcal{S}}$ is denoted by a filled square. The value of φ at $\mathbf{x}$ can be obtained by computing $\rho(\theta_x,\phi_x)$ via biquartic interpolation so

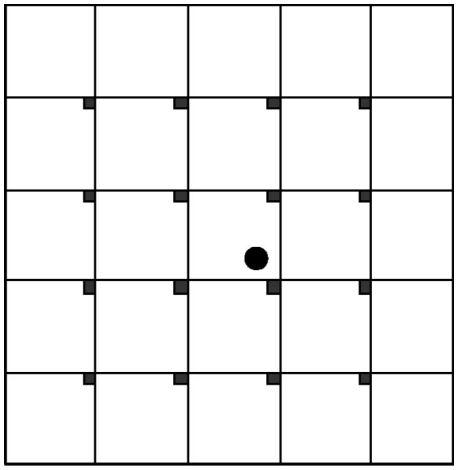

FIG. 17. The choice of stencil points for biquartic interpolation for interpolation points that are on the interior of the grid. The interpolation point is labelled by a filled circle and the mesh points that are used as an interpolation stencil are denoted by filled squares.

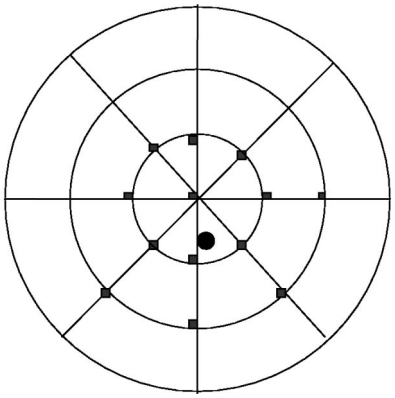

FIG. 18. This figure shows the choice of stencil points for biquartic interpolation for interpolation points that are near the poles. We view the pole points from a 3-dimensional perspective where the identifications of points in the ϕ direction is taken into account. This leads to the special choice of interpolation stencil points as shown. This leads to fourth order truncation error in the interpolant at the poles. The interpolation point is labelled by a filled circle and the mesh points that are used as an interpolation stencil are denoted by filled squares.

that the truncation error has a leading order term which is fourth order in the grid spacing h. The interpolation is carried out with values of $\hat{\rho}$ defined on mesh points of $\hat{\mathcal{S}}$ using a 16 point stencil. Figure 17 shows the choice of these stencil points in the interior of the mesh. At the poles a special choice is made of stencil points which takes into account the indentifications made at the poles. Figure 18 shows a choice of stencil points for an interpolation point near the pole. This approach leads to a fourth order truncation error in $\rho(\theta_x,\phi_x)$ at all points on $\hat{\mathcal{S}}$. Then φ can be constructed for every $\mathbf{x}\in\mathcal{N}$ as $\varphi=r_x-\rho(\theta_x,\phi_x)$. Using this approach φ is defined at any finite difference stencil point for every mesh point on $\hat{\mathcal{S}}$. The finite difference expressions for $\Delta_i^h\varphi$, $\Delta_i^h\Delta_j^h\varphi$ (corresponding to first and second derivatives) are computed at each of the mesh points. The residual is then evaluated on $\hat{\mathcal{S}}$ using these finite difference approximations for the derivatives to $O(h^2)$, and metric data $(\gamma_{ij},\partial_k\gamma_{ij},K_{ij})$ which are specified either analytically or interpolated from an enveloping 3D Cartesian grid.

Because we use $O(h^2)$ finite difference approximations $\Delta_i^h\varphi$, $\Delta_i^h\Delta_j^h\varphi$ to the derivatives, this approach leads to an $O(h^2)$ truncation error in evaluating $\hat{F}[\hat{\rho}]$. Because of our special attention to points near the pole, $\hat{F}$ is evaluated smoothly everywhere on $\hat{\mathcal{S}}$.

With a means for evaluating $\hat{F}$ at any point in the domain of $\hat{S}$ it is straightforward to generate $\hat{J}_{\overline{\mu\nu}}$ numerically using Eq. (9). The algorithm for this is summarized as follows:

Specify metric data everywhere on $\hat{\mathcal{S}}$
Evaluate $\hat{F}[\hat{\rho}]$ everywhere on $\hat{\mathcal{S}}$
For each point (labeled by $\overline{\nu}$) in $\hat{\mathcal{S}}$
  Perturb $\hat{\rho}_{\overline{\nu}}=\hat{\rho}_{\overline{\nu}}+\epsilon$
  Specify metric data on perturbed point
  Evaluate $\hat{F}[\hat{\rho}_{\overline{\nu}}+\epsilon]$ at the $\overline{\mu}$th point.

Compute the $\overline{\mu\nu}$ component of the Jacobian matrix using Eq. (9)

End loop over points on $\hat{\mathcal{S}}$.

This gives the Jacobian matrix, $\hat{J}_{\overline{\mu\nu}}$, for $\hat{F}$ evaluated. $\hat{J}_{\overline{\mu\nu}}$ is a $(N_s^2-2N_s+2)\times(N_s^2-2N_s+2)$ matrix which is used in Newton's method as follows:

Start with an initial guess surface $\hat{\rho}=\hat{\rho}_0$
while $\|\hat{F}\|>$ stopping criterion
Compute the Jacobian $\hat{J}_{\overline{\mu\nu}}$ for the current $\hat{\rho}$
Evaluate $\hat{F}[\hat{\rho}]$
Solve $\hat{J}\cdot\delta\hat{\rho}=-\hat{F}[\hat{\rho}]$ for $\delta\hat{\rho}$
Update the surface $\hat{\rho}=\hat{\rho}+\delta\hat{\rho}$.

[1] J.W. York, in *Frontiers in Numerical Relativity*, edited by C. R. Evans, L. S. Finn, and D. W. Hobill (Cambridge University Press, Cambridge, England, 1989).
[2] S. Hawking and G. Ellis, *The Large Scale Structure of Space-Time* (Cambridge University Press, Cambridge, UK, 1973).
[3] R. Wald and V. Iyer, Phys. Rev. D **44**, 3719 (1991).
[4] T. Nakamura, Y. Kojima, and K. Oohara, Phys. Lett. **106A**, 235 (1984).
[5] N.T. Bishop, Gen. Relativ. Gravit. **14**, 717 (1982).
[6] P. Anninos, K. Camarda, J. Libson, J. Masso, E. Seidel, and W.-M. Suen, Phys. Rev. D **58**, 024003 (1998).
[7] T. Baumgarte, G.B. Cook, M.A. Scheel, S.L. Shapiro, and S.A. Teukolsky, Phys. Rev. D **54**, 4849 (1996).
[8] J. Thornburg, Phys. Rev. D **54**, 4899 (1996).
[9] K.P. Tod, Class. Quantum Grav. **8**, L115 (1991).
[10] D.H. Bernstein, ''Notes on the mean curvature flow method for finding apparent horizons.''
[11] E. Pasch, *SFB 382* Report No. 63, 1997.
[12] D. Shoemaker, M.F. Huq, and R.A. Matzner, Phys. Rev. D **62**, 124005 (2000).
[13] C. Gundlach, Phys. Rev. D **57**, 863 (1998).
[14] M. Alcubierre, S. Brandt, B. Bruegmann, C. Gundlach, J. Masso, E. Seidel, and P. Walker, Class. Quantum Grav. **17**, 2159 (2000).
[15] We define the L_2 norm of an N-component vector $\mathbf{v}$ as follows: $\|\mathbf{v}\|_2\equiv(N^{-1}\Sigma_{i=1}^{N}v_i{}^2)^{1/2}$.
[16] J. Ortega and W. Rheinboldt, *Iterative Solution of Nonlinear Equations in Several Variables* (Academic Press, New York, 1970).
[17] J.J. Dongarra, J.R. Bunch, C.B. Moler, and G.W. Stewart, *LINPACK: Users' Guide* (Society for Industrial and Applied Mathematics, Philadelphia, 1978).
[18] D.S. Kershaw, J. Comput. Phys. **26**, 43 (1978).
[19] S. Klasky, M. Choptuik, and Richard A. Matzner, ''Interpolators/Extrapolators for AMR Finite Difference Codes,'' Technical Report, Center for Relativity, University of Texas at Austin, 1995.
[20] M.F. Huq, *Third Texas Workshop on 3-Dimensional Numerical Relativity* (The University of Texas at Austin, Austin, 1995).
[21] R. Courant, K.O. Friedrichs, and H. Lewy, Math. Ann. **100**, 32 (1928) [English translation of ''Über die Partiellen Differenzengleichungen der Mathematischen Physik'']; IBM J. Res. Dev. **11**, 215 (1967).
[22] C.W. Misner, K.S. Thorne, and J.A. Wheeler, *Gravitation* (W.H. Freeman, New York, 1973).
[23] M.F. Huq, ''Apparent Horizon Location in Numerical Spacetimes,'' Ph.D. dissertation, The University of Texas at Austin, 1996.